Computers and Chemical Engineering 71 (2014) 467–477

Contents lists available at ScienceDirect

Computers and Chemical Engineering

journal homepage: www.elsevier.com/locate/compchemeng

An adaptive moving grid method for solving convection dominated transport equations in chemical engineering

R. Kelling[a,*], J. Bickel[a], U. Nieken[a], P.A. Zegeling[b]

[a] Institute of Chemical Process Engineering, Boeblinger Str. 78, 70199 Stuttgart, Germany
[b] Department of Mathematics, P.O. Box 80010, 3508 TA Utrecht, The Netherlands

ARTICLE INFO

Article history:
Received 19 May 2014
Received in revised form 5 September 2014
Accepted 12 September 2014
Available online 22 September 2014

Keywords:
Dynamic simulation
Adaptive grid
Deacon process
Three-way catalyst
MATLAB
DIANA

ABSTRACT

Convection dominated processes in chemical engineering are frequently accompanied by steep propagating fronts. Numerical simulation of corresponding models with uniform fixed grids requires an excessive amount of grid points along the expected range of the front movement. In this contribution the implementation of an efficient adaptive grid method is presented and applied to two relevant spatially one-dimensional cases, the chlorination stage of the Deacon process and oxygen storage processes in a three-way catalyst. The algorithm exhibits a high accuracy with a much lower number of grid points and a therefore reduced computational effort as opposed to a fixed grid simulation. The present work demonstrates that the algorithm allows for a robust, simple, and fast implementation of the adaptive grid method in common simulation tools and, together with adequate supplementary material, aims to make the method readily accessible to the interested reader.

1. Introduction

Many convection dominated processes in chemical engineering, especially industrial scale applications, are characterized by the formation of steep moving fronts (Eigenberger et al., 2007). A well-known example is the propagation of a thermal and a reaction front during an endothermic or exothermic reaction in a tubular packed bed. Traveling fronts are common phenomena in adsorption columns, ion exchangers, regenerative heat exchangers, or membrane reactors.

The numerical simulation of steep moving fronts or shock fronts with adequate accuracy in time and space is computationally expensive. Many adaptive methods are available to rearrange the grid points according to the local errors of the partial differential equations describing such systems. This allows reducing the number of grid points and therefore the number of equations and the computational cost. Desirable requirements for such methods are a straightforward and easy adaptation of the adaptive grid to the actual physical problem and a fast implementation of the algorithm in common simulation tools. The method has to find high local gradients automatically without an a priori specification of their temporal position, using general grid defining parameters. In this paper we present such a technique using the adaptive grid method as developed in Zegeling (2007) and van Dam and Zegeling (2010) for two typical, spatially one-dimensional models of chemical engineering applications. The models are solved on a moving grid by established simulation tools (MATLAB©, DIANA (Krasnyk et al., 2006)) which provide efficient and robust solvers.

In Section 2 we classify the presented adaptive grid method and describe the main steps of implementation for a general model. In Section 3 the adaptive grid is used to simulate the chlorination stage of the Deacon process. Here, chlorine is stored in a fixed bed leading to a decrease of the total gas flow. The resulting steep fronts make it difficult to carry out an accurate and efficient numerical simulation of this process with uniform grids. In Section 4 we analyze traveling fronts during oxygen storage in a three-way catalyst. Both models are used to provide practical implementation remarks and investigate the performance of the adaptive grid method.

2. Adaptive grid method

In this section we classify the presented adaptive method and describe the algorithmic structure corresponding to its key ingredients: discretization and transformation of the balance equations, the grid defining equation with corresponding parameters, and the monitor function. Although the method handles problems in more than one dimension (Zegeling, 2007; Zegeling et al., 2005; Zegeling

* Corresponding author. Tel.: +49 711 685 85247.
E-mail addresses: rene.kelling@icvt.uni-stuttgart.de, kelling.rene@googlemail.com (R. Kelling).

http://dx.doi.org/10.1016/j.compchemeng.2014.09.011
0098-1354/

Notation

Latin letters

A	reactor cross-section area
B	left hand side matrix of grid equation
c	concentration
c_p	specific heat capacity
D	coefficient of dispersion
E_A	activation temperature
Δh_r	heat of reaction
k^∞	rate constant
L	reactor length
$\dot{m}$	mass flow
MW	molar mass
n	number of grid points
OSC	oxygen storage capacity
OSL	oxygen storage level
p	partial pressure
q	quality of a solution
ROL	relative oxygen level
r	reaction rate per unit of reactor volume
s	steepness of a front
s	right hand side vector of grid equation
t	time
T	temperature
TWC	three-way catalyst
u	states
v_R	velocity of reaction front
w	mass fraction
x	spatial coordinate

Greek letters

α	monitor regularizing parameter
ϵ	volume fraction gas phase
θ	transformed time
λ	axial heat conduction
ν	transformed states
ξ	uniform computational coordinate
σ	spatial smoothing parameter
ρ	density
τ	time smoothing parameter
ω	monitor function

Superscripts

G	gas
S	solid

Subscripts

0	initial
i	index for each grid point
in	inlet
s	index for each state
exh	exhaust

and Kok, 2004), we focus on one-dimensional models for a better understanding of the basic principle.

2.1. Classification of the method

In combination with the method of lines, the discretization in space is carried out using an adaptive grid while the solution in time is obtained with an appropriate solver for the resulting differential-algebraic equation system (DAE). Regarding the implementation of the adaptive grid, different strategies can be applied (Huang and Russel, 2011). To locally increase the grid resolution, mesh cells can be divided into smaller cells by adding grid points (h-refinement). This method is disadvantageous if the number of DAEs has to be fixed for the simulation process (as is the case in several numerical tools). During the so-called r-refinement, which is used in the presented method, the grid nodes are moved to increase local resolution and the number of grid points remains constant. Besides, static and dynamic regridding is distinguished. In static regridding the grid adapts after each time step whereas in the here considered dynamic regridding the adaption is made during each step, which is powerful for traveling fronts and results in larger time steps (Nowak et al., 1996). The presented adaptive method applies a monitor based grid definition equation, using features of the underlying balance equations (physical states) and mesh quality measures. The method is described in the following.

2.2. Discretization and transformation of balance equations

In order to model chemical engineering processes, balance equations (1) for each model state u (e.g. temperature or concentrations) together with corresponding initial conditions (2) can be derived. In the resulting system of partial differential equations (PDEs) the right hand side f does, in general, depend on a function of the states, the time t, the spatial coordinate x and spatial derivatives of the states.

$$\frac{\partial u}{\partial t} = f(u, t, x), \tag{1}$$

$$u(x, t = 0) = u_o(x). \tag{2}$$

In the present case, the PDEs describing the systems considered are parabolic PDEs, consisting of an accumulation term $a(u, t, x)$, a convective term $b(u, t, x)$, a dispersion term $c(u, t, x)$, and a nonlinear reaction source term $d(u, t, x)$:

$$a(u, t, x)\frac{\partial u}{\partial t} = -b(u, t, x)\frac{\partial u}{\partial x} + \frac{\partial}{\partial x}\left(c(u, t, x)\frac{\partial u}{\partial x}\right) + d(u, t, x). \tag{3}$$

To numerically approximate the solution of the resulting PDE system, the spatially dependent variable is discretized along n grid points x_i in the method of lines approach:

$$x = (x_1 = 0, \ldots, x_i, \ldots, x_n = L)^T. \tag{4}$$

Due to the underlying physical processes, steep moving fronts of some states such as temperature and concentration fronts may arise. Consequently, a uniform fixed distribution of the grid points x_i is highly inefficient regarding the computational cost to resolve these fronts. Thus, we apply a technique that is based on a minimization of a so-called mesh-energy integral (Zegeling and Kok, 2004) which distributes the grid points in an adaptive and more efficient way. An additional adaptive grid PDE, describing the movement of the grid, is resulting from this minimization.

The implementation of the adaptive grid is carried out through a coordinate transformation depicted in Fig. 1. The physical (real) solution $u(x, t)$, including 'steep' fronts, is now considered along a non-uniform adaptive coordinate $x(t)$. Through the transformation, this solution is mapped to a computational uniform coordinate system (ξ, θ). Here the solution $\nu(\xi, \theta)$ becomes 'milder'. The balance equations are now considered along this computational coordinate and are therefore easier to solve. To be more precise, the regular transformation (5)–(6) maps the 'steep' solution of the state $u(x, t)$ to a 'mild' computational function $\nu(\xi, \theta)$.

$$\Phi : (x, t) \to (\xi, \theta) \tag{5}$$

$$t(\xi, \theta) = \theta \tag{6}$$

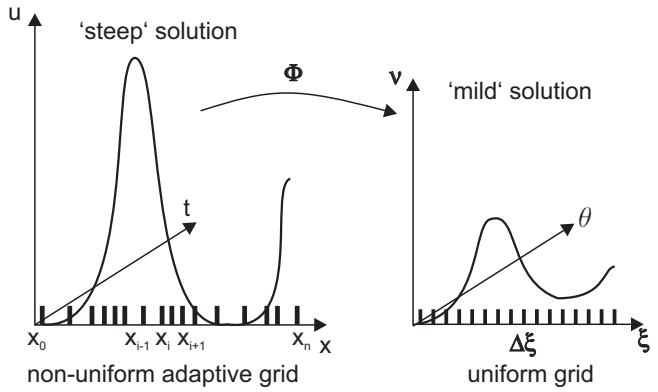

Fig. 1. Discretization in spatial coordinate using the adaptive grid method.

With this transformation the Lagrangian form of the balance equations can be derived (Huang and Russel, 2011):

$$\frac{\partial u}{\partial t} - \frac{\partial u}{\partial x}\frac{\partial x}{\partial t} = f(u, t, x(t)). \tag{7}$$

Now x can be considered as an adaptive moving coordinate $x(t)$. The additional term on the left hand side of Eq. (7) describes the convective grid movement and adapts the particular balance to the moving grid. All model equations which contain time derivatives have to be modified in this way. In case of balance Eq. (3), the transformed equation for the state variables u at the now moving grid points is:

$$a(u, t, x)\left(\frac{\partial u}{\partial t} - \frac{\partial u}{\partial x}\frac{\partial x}{\partial t}\right) = -b(u, t, x)\frac{\partial u}{\partial x} + \frac{\partial}{\partial x}\left(c(u, t, x)\frac{\partial u}{\partial x}\right) + d(u, t, x). \tag{8}$$

The necessary additional grid equation describing $\frac{\partial x}{\partial t}$ is discussed below. The system of balance equations (8) together with the mentioned grid equation can again be solved by the method of lines, using difference quotients according to an appropriate discretization scheme. Second order central differences turned out as suitable approximation for the new convective term in the balance equations. Together with the discretized grid equation (see below) a set of ordinary differential-algebraic equations in time at each (now dynamically changing) grid point $x_i(t)$ is obtained. The solution is usually calculated using a suitable DAE-solver.

2.3. Grid equation

The grid equation describes the dynamic change of the vector of grid points $\partial x/\partial t$ as introduced above. To enable smoothness in time as well as a controlled grid behavior in space, the following general form of the grid equation has been derived:

$$\tau \quad B \quad \frac{\mathrm{d}x}{\mathrm{d}t} = s(u, t, x), \tag{9}$$

$$x(t = 0) = x_0. \tag{10}$$

To initialize the grid, a uniform initial distribution of the grid points is used. In the following only a short summary of the derivation is given. The details of the procedure can be found in Verwer et al. (1988).

The basic idea behind the grid equation is to adaptively distribute a fixed number of grid points over the spatial coordinate, fulfilling the following two important requirements:

- Concentrate grid points in regions with large spatial derivatives.
- Control the adaptivity of the grid to enable a smooth grid distribution.

For the first requirement, the so-called monitor function ω is introduced. It is a summation of spatial derivatives of model states and appears both in the matrix B and the vector s of the right hand side (see Eq. (40) in Appendix A). When this function has a large value, the distance between neighboring grid points has to be low and vice versa (de and Boor, 1974). In our case we used a combination of only first order spatial derivatives as monitor function:

$$\omega = \sum_s \left|\frac{\partial u_s}{\partial x}\right| + \alpha_s(t). \tag{11}$$

First order derivatives are proven as appropriate and highly efficient from a computational point of view (Blom and Verwer, 1989). The monitor function defines a single model state or a combination of different model states u_s, to which the grid has to adapt. The proper selection of adequate states for the monitor function is crucial in order to enable an appropriate grid behavior, as will be shown in the following example. The so-called monitor regularization parameters α_s are added to ensure that the monitor function is strictly positive, because it appears in the denominator of different elements of the matrix B and vector s. For states with very flat gradients the spatial derivatives tend to zero, but the monitor function should still consider these states. If α_s dominates the monitor function, a uniform grid distribution results. To calculate suitable regularizing parameters for a certain state, Eq. (12) can be used (van Dam and Zegeling, 2010):

$$\alpha_s(t) = \int_0^L \left|\frac{\partial u_s}{\partial x}\right| \mathrm{d}x. \tag{12}$$

As outlined in detail in the Appendix A, matrix B couples five temporal derivatives of the grid points to enable a smooth grid distribution in time. The grid equation also contains the *time smoothing parameter* τ which determines how fast the grid reacts on changes of the model in time. If τ tends to infinity, the grid is not adaptive and the initial uniform grid remains. If τ is too small, grid points will adapt too quickly to the solution causing oscillations in time. Thus, a wrong choice of τ can result in starting problems. The time constant τ is related to the critical time scale of the model. A typical value is $\tau = 10^{-3}$, if the time scale of the model is of first order.

The Matrix B and the vector s depend on another parameter, the *spatial smoothing parameter* σ. It determines the minimum and maximum ratio of two adjoining grid points according to Eq. (13).

$$\frac{\sigma}{\sigma + 1} \quad < \quad \frac{\Delta x_{i+1}}{\Delta x_i} = \frac{x_{i+2} - x_{i+1}}{x_{i+1} - x_i} \quad < \quad \frac{\sigma + 1}{\sigma} \tag{13}$$

For the presented applications we used $\sigma = 2$ which defines $2/3 < \Delta x_{i+1}/\Delta x_i < 3/2$.

3. Application I: Deacon-process

3.1. Background of the process

A brief introduction to the Deacon-process and the mathematical model used is given in Nieken and Watzenberger (1999). During the Deacon-process HCl is recycled to chlorine by reaction with oxygen (14).

$$2\,\mathrm{HCl} + \frac{1}{2}\,\mathrm{O_2} \quad \leftrightharpoons \quad \mathrm{Cl_2} + \mathrm{H_2O} \tag{14}$$

A copper chloride catalyst in a fixed-bed reactor is used at temperatures around 450 °C. Although this route looks promising, there are problems with catalyst deactivation and equilibrium limitation to

less than 84% at 350 °C, causing unwanted byproducts which have to be separated from the product stream. Thus, two-stage processes have been proposed (Deacon, 1875; Agar et al., 1997). Here, the catalyst fixed bed is used as chlorine storage during the chlorination stage (15). By means of oxygen the chlorine is removed during the dechloration stage (16), the copper is oxidized and the cycle can start again.

$$2\,HCl + CuO \rightarrow CuCl_2 + H_2O \tag{15}$$

$$CuCl_2 + \frac{1}{2}O_2 \rightarrow CuO + Cl_2 \tag{16}$$

Equilibrium limitations are avoided by this storage effect. In the following, the adaptive grid method is applied to the chlorination stage only. For this purpose the mathematical model suggested in Nieken and Watzenberger (1999) has been adopted.

3.2. Model for chlorination stage

A quasi-homogeneous one-dimensional model of a tubular reactor is used. It is assumed that there is no loss of copper. The balance equations (17)–(22) with corresponding Dankwerts boundary conditions and initial conditions are considered.

$$\epsilon\rho^G \frac{\partial w_{HCl}}{\partial t} = -\frac{\dot m}{A}\frac{\partial w_{HCl}}{\partial x} + D\frac{\partial^2 w_{HCl}}{\partial x^2} - w_{HCl}\frac{1}{A}\frac{\partial \dot m}{\partial x} - 2MW_{HCl}\,r \tag{17}$$

$$\epsilon\rho^G \frac{\partial w_{H_2O}}{\partial t} = -\frac{\dot m}{A}\frac{\partial w_{H_2O}}{\partial x} + D\frac{\partial^2 w_{H_2O}}{\partial x^2} - w_{H_2O}\frac{1}{A}\frac{\partial \dot m}{\partial x} + MW_{H_2O}\,r \tag{18}$$

$$(1-\epsilon)\rho^S c_p^S \frac{\partial T}{\partial t} = -\frac{\dot m}{A}c_p^G\frac{\partial T}{\partial x} + \lambda\frac{\partial^2 T}{\partial x^2} - c_p^G T\frac{1}{A}\frac{\partial \dot m}{\partial x} - \Delta h_r\,r \tag{19}$$

$$(1-\epsilon)\frac{\partial c_{CuCl_2}}{\partial t} = r \tag{20}$$

$$(1-\epsilon)\frac{\partial c_{CuO}}{\partial t} = -r \tag{21}$$

$$0 = -\frac{1}{A}\frac{\partial \dot m}{\partial x} + r\,(MW_{CuO} - MW_{CuCl_2}) \tag{22}$$

They contain the component mass balances for the gaseous species (hydrogen chloride w_{HCl} and water w_{H_2O}) and the enthalpy balance to calculate the temperature with accumulation, convection, dispersion, and reaction source terms. Convection and dispersion are neglected in the mass balances of the immobilized solids (copper chloride c_{CuCl_2} and copper oxide c_{CuO}). The mass flow is changing due to storage and release of chlorine in the solid phase. To describe this effect the quasi stationary total mass balance (22) is used. Reaction rates and model parameters are listed in the Appendix A.

The first order spatial derivatives are discretized with first-order backward differences (23) and the second order derivatives with second-order central differences (24).

$$\left.\frac{\partial u}{\partial x}\right|_i \approx \frac{u_i - u_{i-1}}{x_i - x_{i-1}} \tag{23}$$

$$\left.\frac{\partial^2 u}{\partial x^2}\right|_i \approx \frac{2\,u_{i-1}}{(x_{i-1}-x_i)(x_{i-1}-x_{i+1})} + \frac{2\,u_i}{(x_i - x_{i-1})(x_i - x_{i+1})} + \frac{2\,u_{i+1}}{(x_{i+1}-x_{i-1})(x_{i+1}-x_i)} \tag{24}$$

The model is implemented in ProMoT (Mirschel et al., 2009) enabling the simulation with the IDA-solver from SUNDIALS (Hindmarsh et al., 2005), using the dynamic simulation and numerical analysis tool DIANA (Krasnyk et al., 2006). The approximation in time is carried out with variable-order, variable-coefficient backward differences. The solution of the resulting nonlinear system is accomplished with a modified Newton iteration.

3.3. Results with an equidistant grid

Fig. 2 shows axial profiles of significant model states after 8, 16, 24 and 32 s for simulations with 100 (–○–) and 1000 (–•–) equidistant grid points. To understand the process of chlorination we first consider the simulation with 1000 grid points. We start with a uniformly preheated reactor filled with 1 kmol/m^3 CuO. Hydrogen chloride mixed with nitrogen is fed at a temperature of 300 °C. A steep reaction front propagates through the reactor. In the reaction front HCl (Fig. 2(a)) and CuO (Fig. 2(b)) are consumed and the temperature rises above 400 °C (Fig. 2(c)). Due to chlorine storage the mass flow is reduced considerably in the reaction front from 0.2 to 0.15 kg/s (Fig. 2(d)). After breakthrough of the reaction front, the feed concentrations are present in the gas phase and the CuO is completely reduced to $CuCl_2$. The inlet temperature is reached with a second front, hereinafter referred to as thermal front, which is slower than the reaction front.

Interestingly, there are considerable differences between the solutions using 100 and 1000 grid points. The velocity of the reaction front for the 100 grid points solution (v_R = 0.01225 m/s) is significantly lower than the front velocity of the 1000 grid points solution (v_R = 0.01338 m/s). This is due to the fact that the better resolved steep front on the dense grid results in a stronger contribution of the dispersion terms which accelerate the front movement. The considered model consequently imposes tough requirements on the spatial resolution of the grid. While the resolution of the steep fronts is much better for 1000 uniform distributed points, most of the grid points are located upstream or downstream from the front, where they are not required since no gradients exist.

3.4. Results with the adaptive grid

The monitor function is crucial for the adaptive grid behavior and the quality of the simulation results. Therefore, an appropriate model state or combination of states has to be chosen in order to adapt the grid as good as possible to the model behavior. Fig. 2 shows the shapes of the fronts. The front of the gas components mass fraction (cf. HCl mass fraction Fig. 2(a)) is S-shaped in contrast to the front of the mass flow and the solid components concentration (cf. CuO concentration Fig. 2(b)) which is half S-shaped and steeper. The temperature profile contains two fronts, the half S-shaped reaction front mentioned before and the less steep S-shaped thermal front. The thermal front is curved opposite to the reaction front.

To cover the complete S-shape of the reaction front with grid points the mass fraction of HCl is taken as monitor function for the first adaptive grid simulation and the monitor regularizing parameter $\alpha(t)$ is calculated with the integral (12):

$$\omega = \left|\frac{\partial w_{HCl}}{\partial x}\right| + \underbrace{\int_0^L \left|\frac{\partial w_{HCl}}{\partial x}\right| dx}_{\alpha(t)}. \tag{25}$$

The grid equation is implemented with the spatial smoothing parameter $\sigma = 2$ and the temporal smoothing parameter $\tau = 10^{-3}$ as recommended in the literature (Zegeling, 2007). These values are used in all adaptive grid simulations in this contribution. The

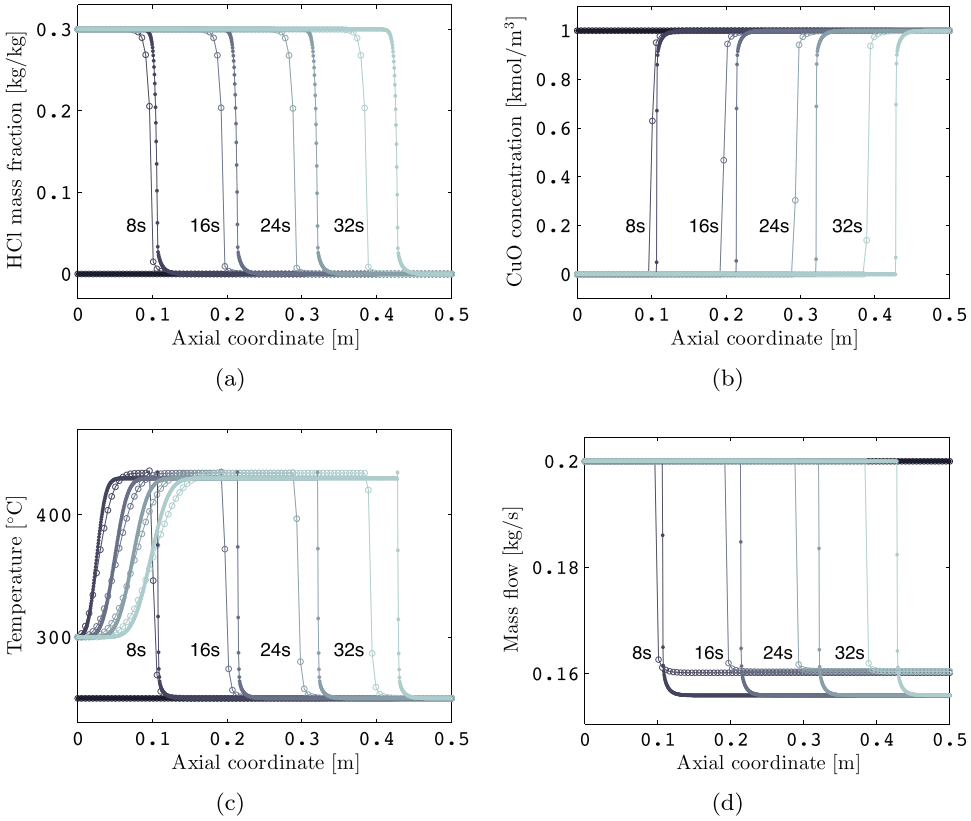

Fig. 2. Deacon process: Chlorine storage simulation using an equidistant fixed grid with 100 grid points (–○–) and 1000 grid points (–•–).

left-hand sides of the model equations are adapted according to equation (7) as follows:

$$\epsilon\rho^G \frac{\partial w_j}{\partial t} \to \epsilon\rho^G \left(\frac{\partial w_j}{\partial t} - \frac{\partial w_j}{\partial x}\frac{\partial x}{\partial t} \right) \tag{26}$$

$$(1-\epsilon) \frac{\partial c_j}{\partial t} \to (1-\epsilon) \left(\frac{\partial c_j}{\partial t} - \frac{\partial c_j}{\partial x}\frac{\partial x}{\partial t} \right) \tag{27}$$

$$(1-\epsilon)\,\rho^S c_p^S \frac{\partial T}{\partial t} \to (1-\epsilon)\,\rho^S c_p^S \left(\frac{\partial T}{\partial t} - \frac{\partial T}{\partial x}\frac{\partial x}{\partial t} \right). \tag{28}$$

The model and simulation code is attached as supplementary material of this publication.

The results of the adaptive grid simulation are shown in Fig. 3 (left). As expected, most of the grid points are located on the reaction front (Fig. 3(a)). Fig. 3(c) shows the corresponding temperature profiles. The reaction front is described very well with the adaptive grid in contrast to the less resolved thermal front. Fig. 3(d) shows the grid distribution at various points in time. Initially the grid is uniform. During the first time interval about one third of the grid points move to the reaction front. They follow the reaction front (arrow) for 36 s. After breakthrough of the front the grid becomes uniform again.

To improve the temperature profiles and map the thermal front with more adaptive grid points the temperature is chosen as additional monitor in the second simulation:

$$\omega = \left|\frac{\partial w_{\mathrm{HCl}}}{\partial x}\right| + \int_0^L \left|\frac{\partial w_{\mathrm{HCl}}}{\partial x}\right| \mathrm{d}x + \left|\frac{\partial T}{\partial x}\right| + \int_0^L \left|\frac{\partial T}{\partial x}\right| \mathrm{d}x. \tag{29}$$

Here, the reaction front as well as the thermal front is mapped with about one third of the grid points respectively. Fig. 3(c) illustrates the nice adaptivity of the grid to the temperature. However, the S-shaped front of the gas component HCl (in Fig. 3(b)) is described with many grid points being located on the right-hand side of the front but only few on the front itself. Fig. 3(e) shows that the grid follows two propagating fronts. After 43 s the reaction front breaks through and most of the grid points move to the slower thermal front.

Comparing this grid with Fig. 3(d), where the HCl mass fraction was used as monitor function, it can be seen that the propagation velocity of the reaction front is now higher ($v_R = 0.01358$ m/s versus $v_R = 0.01185$ m/s). Through the position of the grid points, the monitor function does therefore also affect the front velocity. Fig. 4 compares three different simulation strategies for different numbers of grid points, the uniform (equidistant) grid, the adaptive grid with $\omega = w_{\mathrm{HCL}}$ (Eq. (25)) and the adaptive grid with ω according to Eq. (29). Since the absolute values of w_{HCL} and T are about three orders of magnitude apart, in the latter case ω is almost exclusively dominated by T. The actual propagation velocity is analytically predictable using Eq. (30) (Kolios, 2013).

$$v_R \approx \frac{\dot{m}_{in}\, w_{\mathrm{HCl},in}}{2\ \ A\ \ (1-\epsilon)\, c_{\mathrm{CuO},0}\, MW_{\mathrm{HCl}}} = 0.013717\,\mathrm{m/s} \tag{30}$$

Even at a small number of grid points, the adaptive grid with w_{HCl} as monitor function shows a good agreement with the analytical solution. A total number of about 25–50 adaptive points is sufficient to reach the same accuracy (measured by front velocity) as with 2000 equidistant grid points. Using mainly the temperature as monitor as in Eq. (29), the accuracy is worse than for the uniform grid. Therefore, the monitor function plays a crucial part in the precision of the solution. In the present case, the obvious solution for a better monitor function than Eq. (29) would be to use relative values $w_{\mathrm{HCl}}/w_{\mathrm{HCl,in}}$ and T/T_{in} instead of the absolute values. This would place more grid points in the concentration front.

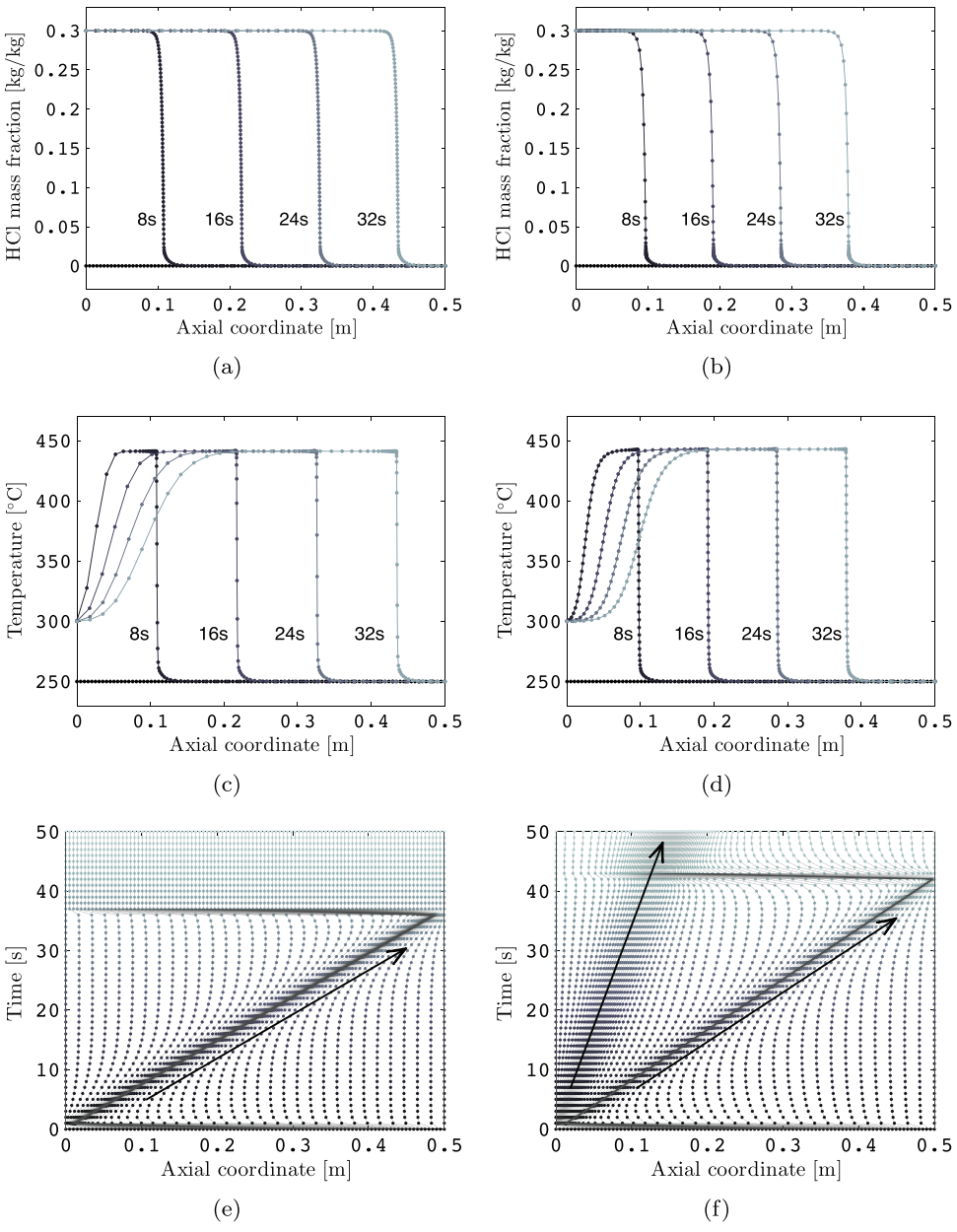

Fig. 3. Deacon process: Chlorine storage simulation using the adaptive grid with 100 grid points. Hydrogen chloride mass fraction w_{HCl} as monitor function (left) and temperature as monitor function (right).

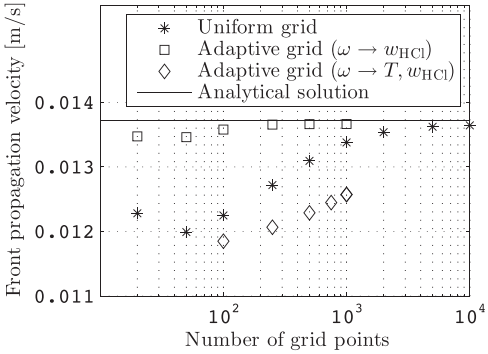

Fig. 4. Deacon process: front propagation velocity for different number of grid points and simulation strategies.

4. Application II: three-way catalyst

4.1. Background

Three-way catalysts (TWCs) are mainly used to reduce the emissions of gasoline powered spark-ignition engines. When operated with a stoichiometric mixture of gasoline and oxygen, a TWC is able to both catalyze the oxidation of carbon monoxide (CO) and hydrocarbons (HC) as well as the reduction of nitrogen oxides (NO_x). However, maintaining a stoichiometric mixture under all driving conditions is impossible. Therefore, oxygen storage materials have been incorporated into the washcoat of TWCs. While oxidation of the storage material (oxygen storage) takes place during lean operation, a subsequent reduction of the storage material (oxygen release) takes place during rich operation. This essentially enables the TWC to buffer oscillations around stoichiometry and maintain high conversion efficiency during lean-rich cycling.

A widely used method to investigate the dynamics of oxygen storage and release is to subject the TWC to subsequent pulses of O_2 and CO in an inert carrier gas (Usmen et al., 1995; Kašpar et al., 2001, etc.). As present oxygen storage materials such as CeO_2–ZrO_2 mixed oxides do not only possess very high oxygen storage capacities but can also be oxidized and reduced rapidly (Boaro et al., 2004), both the concentrations of CO/O_2 and the fraction of oxidized CeO_2 change rapidly during these tests and a corresponding model has to be able to capture steep concentration fronts. The purpose of the following discussion is to show that using the adaptive grid method introduced above is advantageous for such a model. This is demonstrated by establishing a very simple TWC model describing the principles of oxygen storage and release during a pulse experiment.

4.2. TWC model

For the TWC model, the following reaction scheme is used:

$$O_2 + 2* \xrightarrow{r_{O_2}} 2\,O^* \tag{31}$$

$$CO + O^* \xrightarrow{r_{CO}} CO_2 + *. \tag{32}$$

As the nature of the specific oxygen storage material is not relevant for the present investigation, the reduced state of the material is simply represented by vacant oxygen storage sites *, while the oxidized state is represented by occupied sites O^*. While reaction (31) leads to storage of O_2 from the gas phase, the stored oxygen directly reacts with CO from the gas phase in reaction (32). The amount of oxygen stored as O^* is denoted as the oxygen storage level (OSL) with the oxygen storage capacity (OSC) of the catalyst being the maximum OSL. It is assumed that the storage and release rates are dependent on the reaction rate constants k_{CO} and k_{O_2}, the current OSL, and the mass fractions of CO and O_2 (ω_{CO}/ω_{O_2}) in the following way:

$$r_{O_2} = k_{O_2}\,\omega_{O_2}\,(\mathrm{OSC} - \mathrm{OSL})^2 \tag{33}$$

$$r_{CO} = k_{CO}\,\omega_{CO}\,\mathrm{OSL}. \tag{34}$$

To focus on the phenomena related to oxygen storage and release, a quasi-homogeneous, one-dimensional single-channel model of an isothermal flatbed reactor with quasi-stationary gas phase mass balance equations is used. Furthermore, it is assumed that the exhaust mass flow per unit area $\dot{m}_{exh}$ is constant. This leads to the following system of equations:

$$\frac{\dot{m}_{exh}}{MW_{O_2}}\frac{\partial \omega_{O_2}}{\partial x} = -r_{O_2} \tag{35}$$

$$\frac{\dot{m}_{exh}}{MW_{CO}}\frac{\partial \omega_{CO}}{\partial x} = -r_{CO} \tag{36}$$

$$\frac{\partial \mathrm{OSL}}{\partial t} = MW_{O_2}\left(r_{O_2} - \frac{1}{2}\,r_{CO}\right). \tag{37}$$

As dispersion is neglected, only first-order spatial derivatives appear. They are approximated by first-order backward differences (23) with corresponding boundary conditions at the reactor inlet. The time integration of the resulting DAE system is carried out using the Matlab (version R2014a) ode15s solver. Both the model code and the adaptive grid implementation can be found in the supplementary material of this contribution.

4.3. Simulation setup

To compare the uniform and adaptive grid method, the simulation shown in Fig. 5 is carried out. As it can be seen, the experiment starts with lean operation and no CO in the feed. After 0.5 s a CO pulse of 0.5 s is introduced. During the pulse, O_2 is switched off.

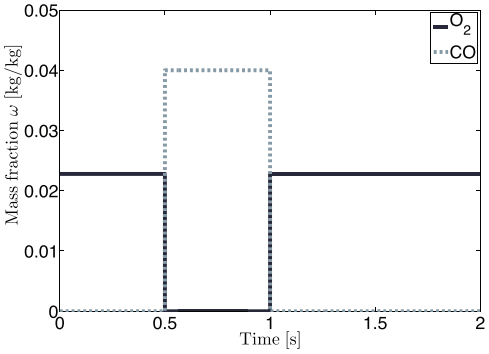

Fig. 5. TWC: pulse experiment. Oxygen and carbon monoxide mass fraction ω_{O_2}/ω_{CO} at the inlet of the TWC.

In the following section, the simulation results using both the uniform and adaptive grid method are compared. Given the fact that either the mass fraction of CO or O_2 are zero during the experiment, one can already conclude that none of them represents a suitable choice for the monitor function of the adaptive grid. Consequently, the OSL is used as monitor function. The parameters determining the behavior of the adaptive grid ($\sigma = 2$, $\tau = 10^{-3}$) are the same as in the case of the deacon process, indicating that the adaptive grid method can be easily adopted to different applications.

4.4. Results

Fig. 6(a) and (b) shows the spatial profiles of the mass fraction of CO and the relative oxygen level ROL during the CO pulse. The ROL represents the fraction of oxidized oxygen storage material and is simply defined as ROL = OSL/OSC.

As it can be seen, the oxygen stored is rapidly depleted by reaction (32) with CO from the gas phase. In the case of the ROL, this results in a sharp S-shaped front propagating from the inlet to the outlet of the reactor. In the case of CO, the S-shape is mirrored. The dots (•) in Fig. 6 are representing the positions of the 40 grid points used for the spatial discretization. In the case of the uniform grid (solid lines), only very few of them are located at the current position of the front. In fact, almost all grid points are located at axial positions where the spatial derivatives of CO and ROL are zero. In contrast to that, using the adaptive grid method (dotted lines) allows the grid points to concentrate on the front. Most notably, this again results in steeper fronts for both the mass fraction of CO and the OSL, which will be discussed in more detail below.

Now the spatial profiles of the mass fraction of O_2 and the relative oxygen level ROL right after the CO pulse will be discussed (Fig. 7(a) and (b)).

As shown in the figure, the rich pulse has not led to a complete depletion of the oxygen stored in the TWC and a breakthrough of CO has been avoided. Near the outlet of the reactor, the shape of the front resulting from the depletion of the ROL (Fig. 6(b)) is therefore preserved until the front resulting from the subsequent storage of oxygen has reached this point (around 1.46 *s* in Fig. 7(b)). Until then, there is constantly a steep S-shaped part in the spatial profile of the ROL at a position of around 0.14 m and a mirrored S-shaped front moving from the inlet to the outlet of the reactor. In the case of the mass fraction of O_2 the spatial profiles are similar to those observed for the mass fraction of CO during the depletion. However, this time a O_2 breakthrough is eventually observed and the front is less steep.

Regarding the steepness, the differences between the solutions using the uniform and the adaptive grid method are less pronounced than in the case of depletion. However, the differences in the current position of the front at a given point in time are more

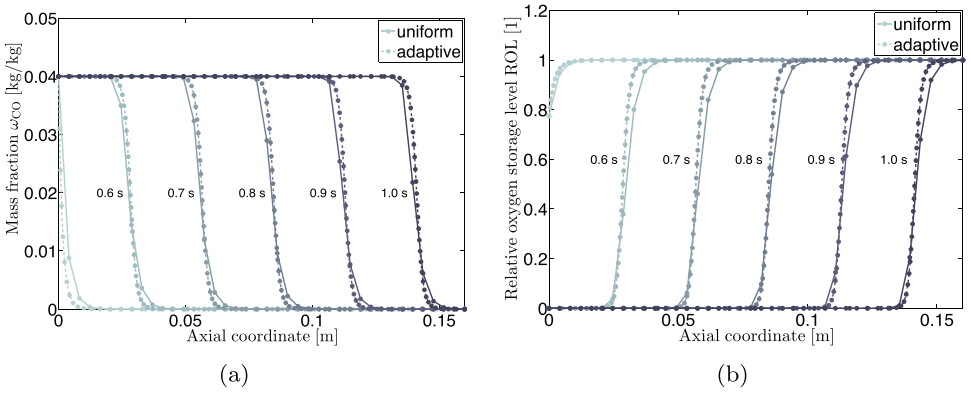

Fig. 6. TWC: depletion. Spatial profiles of the carbon monoxide mass fraction ω_{CO} and the ROL during the CO pulse.

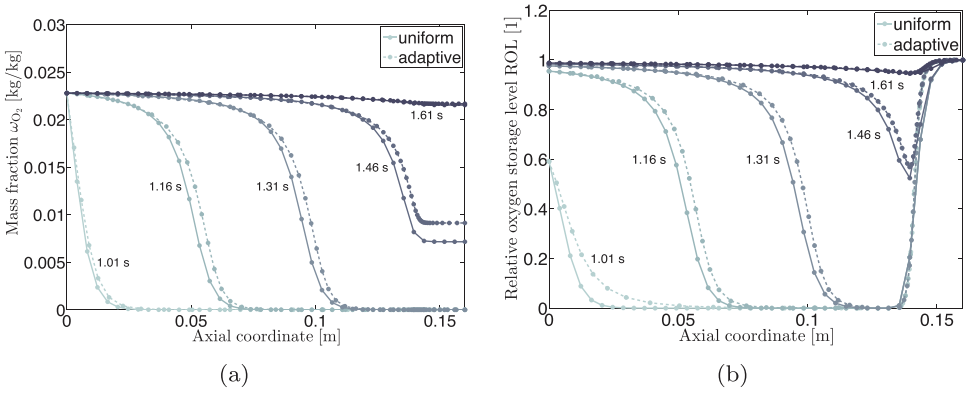

Fig. 7. TWC: storage. Spatial profiles of the oxygen mass fraction ω_{O_2} and the ROL after the CO pulse.

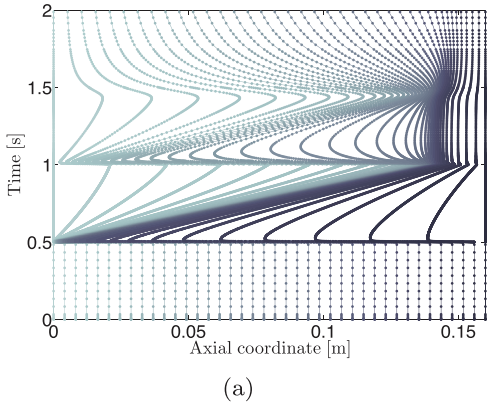

Fig. 8. TWC: grid movement. Location of the grid points during the TWC-simulation shown in Figs. 6 and 7.

obvious. To understand in how far the computation of a solution differs when using the adaptive grid method, the movement of the grid points during the simulation experiment is depicted in Fig. 8. Again, the dots (•) are representing the positions of the 40 grid points.

During the first 0.5 s of the simulation, the grid is equally distributed over the length of the catalyst because the spatial derivatives are zero at all positions. After the introduction of the CO pulse at 0.5 s, the grid points are rapidly moving to the left with a majority of them concentrating near the inlet of the reactor where the steepest spatial gradients appear. During the pulse, this accumulation of grid points moves toward the outlet of the reactor following the fronts shown in Fig. 6. As soon as the pulse is over (1 s), the grid points are again moving to the left. However, this time a large number of grid points stays concentrated near the outlet of the reactor where the constantly steep part of the ROL profile shown in Fig. 7(b) remains. Thus, both this phenomena and the storage front, propagating through the reactor can be well resolved with only 40 grid points. Once the storage front has reached the outlet (around 1.4 s), the grid is beginning to restore a uniform distribution. Overall and as expected, the grid points are always concentrated around steep spatial gradients.

In order to show in how far this grid adaption is advantageous, the depletion front shown in Fig. 6(b) is investigated in more detail. Fig. 9(a) shows the simulation results of the front at 0.75 s. For the fixed grid, a number of grid points of 20, 40, 80, and 160 were used. As expected, the front becomes steeper with an increasing number of grid points. To obtain a solution that is qualitatively equal to the solution using the fixed grid and 160 grid points, only 40 grid points have to be used when the adaptive grid method is employed.

However, one has to keep in mind that the considerable advantage of the adaptive grid comes with a higher computational demand. The computation time (Intel(R) Core(TM)2 Duo CPU E8500 @ 3.16GHz) for the simulation experiment for a varying number of grid points is shown in Fig. 10(a). Clearly, making use of the adaptive grid method leads to unreasonably high computation times if a large number of grid points is used. This is because the solution of the grid equations is computationally expensive. Therefore, both the computation time and the quality of the solution have to be considered.

In order to allow for such a quantitative comparison, the steepness s of the spatial gradient of the ROL in the center of the front

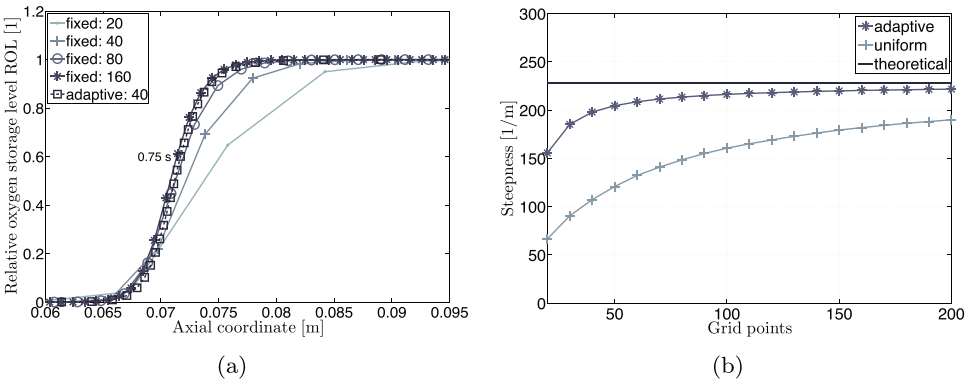

Fig. 9. TWC: steepness. Spatial profile of the ROL at 0.75 s and the spatial gradient of the ROL in the center of the front (ROL = 0.5) for a varying number of grid points.

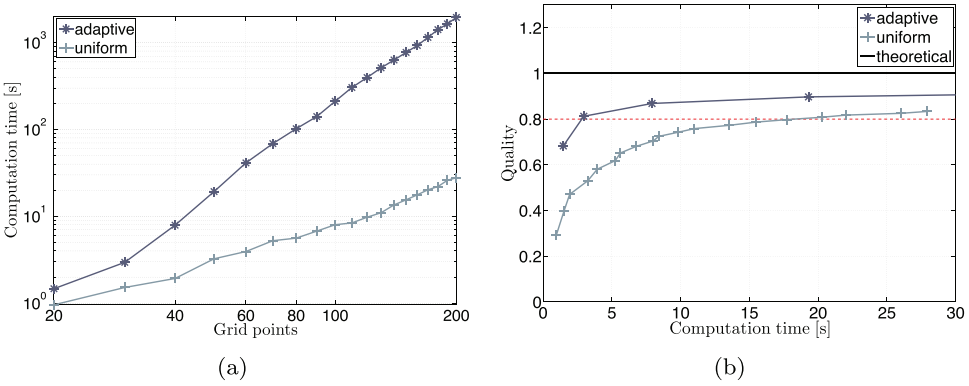

Fig. 10. TWC: quality and computational cost trade-off. Computation time for the simulation experiment for a varying number of grid points and quality of the solution for the respective computation times.

(ROL = 0.5) is calculated both theoretically and numerically for a varying number of grid points. To do so, Eq. (38) is used (Kolios, 2013):

$$s \approx \frac{1/4\, MW_{CO}\, k_{CO}\, \mathrm{OSC}}{\dot{m}_{exh}} = 228.02\, 1/\mathrm{m}. \tag{38}$$

Fig. 9(b) shows the results of the calculation for the uniform and adaptive grid with a number of grid points ranging from 20 to 200. In all cases, the results obtained with the adaptive grid are closer to the theoretical value. However, the deviation between the two methods is becoming smaller with an increasing number of grid points. To connect these results with the computation time, the quality q of the solution may be defined as:

$$q = 1 - \frac{s_{\mathrm{theoretical}} - s_n}{s_{\mathrm{theoretical}}}, \tag{39}$$

where n represents the number of grid points used for the calculation. Fig. 10(b) compares the quality of the solution of both methods for the computation time determined in Fig. 10(a). This demonstrates that using the adaptive grid method can indeed be highly efficient. To achieve a quality of e.g. 80% (dashed line), the adaptive grid is around six times faster.

5. Conclusion

Adaptive moving grids are widely used to improve the efficiency of numerical simulations with respect to the computational effort. The present work describes the implementation of an adaptive grid method recently presented in Zegeling (2007) and van Dam and Zegeling (2010) and investigates its performance when applied to two systems from chemical engineering (Deacon process and three-way catalysts).

Both models are characterized by steep propagating fronts. To resolve the front movement efficiently, the presented method adapts the grid points according to a monitor function, evaluating the gradients of selected state variables. When chosen adequately, it could be shown that, for a given number of grid points, the method clearly outperforms a fixed uniform distribution of the grid points with respect to the model accuracy. This has been shown by comparing the simulation results to analytically obtained values for the front propagation velocity and the steepness of the front.

The increased accuracy is connected to a higher computational effort arising from the solution of the PDEs describing the movement of the grid. However, compared to the fixed grid, a higher or equal model accuracy could be achieved with a much lower number of grid points and, consequently, lower overall computation times.

As additional advantage, the grid implementation is simple and does not require great expenditure of time and effort in adjusting the grid parameters. A priori information about the position of the moving fronts is not required and discontinuities at the inlet boundary are handled with sufficient stability.

Appendix A.

Adaptive grid: grid equation

Eq. (40) shows the matrix B of grid Eq. (9) and the right hand side s. The corresponding coefficients are listed below.

$$B = \begin{pmatrix} 1 & 0 & \dots & & & & & & & 0 \\ 1 & -2 & 1 & 0 & \dots & & & & & 0 \\ b_1 & b_2 & b_3 & b_4 & b_5 & 0 & \dots & & & 0 \\ \vdots & & & & \vdots & & & & & \vdots \\ 0 & \dots & 0 & b_{i-2} & b_{i-1} & b_i & b_{i+1} & b_{i+2} & 0 & \dots & 0 \\ \vdots & & & & \vdots & & & & & \vdots \\ 0 & & & & \dots & 0 & b_{n-4} & b_{n-3} & b_{n-2} & b_{n-1} & b_n \\ 0 & & & & & & \dots & 0 & 1 & -2 & 1 \\ 0 & & & & & & & & \dots & 0 & 1 \end{pmatrix}$$

$$s = \begin{pmatrix} 0 \\ 0 \\ s_3 \\ \vdots \\ s_i \\ \vdots \\ s_{n-2} \\ 0 \\ 0 \end{pmatrix} \tag{40}$$

with

$$\begin{aligned} b_{i-2} &= -\frac{\mu}{\omega_{i-1}\cdot\left(\Delta x_{i-2}\right)^2} \\ b_{i-1} &= \frac{\mu}{\omega_i\cdot\left(\Delta x_{i-1}\right)^2} + \frac{1+2\cdot\mu}{\omega_{i-1}\cdot\left(\Delta x_{i-1}\right)^2} + \frac{\mu}{\omega_{i-1}\cdot\left(\Delta x_{i-2}\right)^2} \\ b_i &= -\frac{\mu}{\omega_i\cdot\left(\Delta x_{i-1}\right)^2} - \frac{1+2\cdot\mu}{\omega_i\cdot(\Delta x_i)^2} - \frac{1+2\cdot\mu}{\omega_{i-1}\cdot\left(\Delta x_{i-1}\right)^2} - \frac{\mu}{\omega_{i-1}\cdot(\Delta x_i)^2} \\ b_{i+1} &= \frac{\mu}{\omega_i\cdot\left(\Delta x_{i+1}\right)^2} + \frac{1+2\cdot\mu}{\omega_i\cdot(\Delta x_i)^2} + \frac{\mu}{\omega_{i-1}\cdot(\Delta x_i)^2} \\ b_{i+2} &= -\frac{\mu}{\omega_i\cdot\left(\Delta x_{i+1}\right)^2} \\ s_i &= \frac{1}{\omega_i}\left(-\frac{\mu}{\Delta x_{i+1}} + \frac{1+2\cdot\mu}{\Delta x_i} - \frac{\mu}{\Delta x_{i-1}}\right) - \frac{1}{\omega_{i-1}}\left(-\frac{\mu}{\Delta x_i} + \frac{1+2\cdot\mu}{\Delta x_{i-1}} - \frac{\mu}{\Delta x_{i-2}}\right) \end{aligned}$$

with

$$\begin{aligned} \Delta x_i &= x_{i+1} - x_i \\ \mu &= \sigma\cdot(\sigma+1) \end{aligned}$$

Deacon-process: equations and parameters

Table A1 contains the model parameters and Table A2 the initial and inlet conditions. The rate of reaction r is determined by a simple power law (41) with the CuO concentration and the partial pressure of hydrogen chloride p_{HCl}:

$$r = k_\infty \mathrm{e}^{-E_a/T} c_{CuO}\cdot p_{HCl} \tag{41}$$

Three-way catalyst: parameters

Table A3 contains the model parameters and Table A4 the initial and inlet conditions.

Table A1
Parameters for chlorination stage of Deacon-process.

Volume fraction gas phase	ϵ	0.4
Reactor length	L	0.5 m
Reactor cross-section area	A	0.1 m^2
Pressure	p	1 bar
Solid density	ρ^S	1500 kg/m^3
Gas density	ρ^G	Ideal gas law
Specific solid heat capacity	c_p^S	0.74 kJ/kg K
Specific gas heat capacity	c_p^G	Nasa polynomials
Axial heat conduction	λ	0.003 kW/m K
Coefficient of dispersion	D	0.005 kg/m s
Heat of reaction	Δh_r	−116,383 kJ/kmol
Activation temperature	E_a	12,000 K
Rate constant	k^∞	5E+10 1/s bar

Table A2
Initial and inlet conditions.

Initial HCl mass fraction	$w_{HCl}(t=0)$	0.0
Initial H_2O mass fraction	$w_{H_2O}(t=0)$	0.0
Initial N_2 mass fraction	$w_{N_2}(t=0)$	1.0
Initial CuO concentration	$c_{CuO}(t=0)$	1.0 kmol/m^3
Initial $CuCl_2$ concentration	$c_{CuCl_2}(t=0)$	0.0 kmol/m^3
Initial temperature	$T(t=0)$	523.15 K
Initial mass flow	$\dot{m}(t=0)$	0.2 kg/s
Inlet HCl mass fraction	$w_{HCl,in}$	0.3
Inlet H_2O mass fraction	$w_{H_2O,in}$	0.0
Inlet temperature	T_{in}	573.15 K
Inlet mass flow	$\dot{m}_{in}$	0.2 kg/s

Table A3
Parameters for three-way catalyst model.

Reactor length	L	0.16 m
Reactor cross-section area	A	0.4148 cm^2
Exhaust mass flow	$\dot{m}_{exh}$	2.78 kg/m^2 s
Oxygen storage capacity	OSC	0.226 kg/m^3
Rate constant	k_{O_2}	8E+5 m^{3}mol/kg^{2}s
Rate constant	k_{CO}	4E+5 mol/kg s

Table A4
Initial and inlet conditions.

Initial O_2 mass fraction	$w_{O_2}(t=0)$	0.0228
Initial CO mass fraction	$w_{CO}(t=0)$	0.0002
Initial oxygen storage level OSL	$w_{OSL}(t=0)$	0.226 kg/m^3
Inlet O_2 mass fraction, lean operation	$w_{O_2,in}$	0.0228
Inlet CO mass fraction, lean operaion	$w_{CO,in}$	0.0
Inlet O_2 mass fraction, rich operation	$w_{O_2,in}$	0.0
Inlet CO mass fraction, rich operaion	$w_{CO,in}$	0.04

Appendix B. Supplementary data

Supplementary data associated with this article can be found, in the online version, at http://dx.doi.org/10.1016/j.compchemeng.2014.09.011.

References

Agar DW, Watzenberger O, Hagemayer A. A novel unsteady state process for HCl-oxidation. In: Reintegration; 1997.
Blom JG, Verwer JG. On the use of the arclength and curvature monitor in a moving-grid method which is based on the method of lines. Technical report. Centre for Mathematics and Computer Science; 1989.
Boaro M, Giordano F, Recchia S, Dal Santo V, Giona M, Trovarelli A. On the mechanism of fast oxygen storage and release in ceria-zirconia model catalysts. Appl Catal B: Environ 2004;52:225–37.
de Boor C. Good approximation by splines with variable knots. II. In: Watson GA, editor. Conference on the numerical solution of differential equations, volume 363 of lecture notes in mathematics; 1974.
Deacon H. Improvement in manufacture of chlorine. U.S. Patent 165,802; 1875.
Eigenberger G, Kolios G, Nieken U. Thermal pattern formation and process intensification in chemical reaction engineering. Chem Eng Sci 2007;62:4825–41.

Hindmarsh AC, Brown PN, Grant KE, Lee SL, Serban R, Shumaker DE, et al. Sundials: suite of nonlinear and differential/algebraic equation solvers. ACM Trans Math Softw 2005;31(September (3)):363–96, http://dx.doi.org/10.1145/1089014.1089020, ISSN 0098-3500.

Huang W, Russel RD. Adaptive moving mesh methods. New York: Springer; 2011.

Kašpar J, Di Monte R, Fornasiero P, Graziani M, Bradshaw H, Norman C. Dependency of the oxygen storage capacity in zirconia-ceria solid solutions upon textural properties. Top Catal 2001;16/17:83–7.

Kolios G. (Habilitation thesis) Regenerative fixed-bed processes: approximative analysis and efficient computation of the cyclic steady state (Habilitation thesis). University of Stuttgart; 2013.

Krasnyk M, Bondareva K, Milokhov O, Teplinskiy K, Ginkel M, Kienle A. The promot/diana simulation environment. In: Marquardt W, Pantelides C, editors. 16th European symposium on computer aided process engineering and 9th international symposium on process systems engineering, volume 21 of Computer aided chemical engineering. Elsevier; 2006. p. 445–50, DOI: 10.1016/S1570-7946(06)80086-6.

Mirschel S, Steinmetz K, Rempel M, Ginkel M, Gilles ED. Promot: modular modeling for systems biology. Bioinformatics 2009;25(5):687–9, http://dx.doi.org/10.1093/bioinformatics/btp029.

Nieken U, Watzenberger O. Periodic operation of the deacon process. Chem Eng Sci 1999;54(13-14):2619–26, http://dx.doi.org/10.1016/S0009-2509(98)00490-4, ISSN 0009-2509.

Nowak U, Frauhammer J, Nieken U. A fully adaptive algorithm for parabolic partial differential equations in one space dimension. Comput Chem Eng 1996;20:547–61.

Usmen RK, Graham GW, Watkins WLH, McCabe RW. Incorporation of La^{3+} into a $Pt/CeO_2/Al_2O_3$ catalyst. Catal Lett 1995;30:53–63.

van Dam A, Zegeling PA. Balanced monitoring of flow phenomena in moving mesh methods. Commun Comput Phys 2010;7:138–70.

Verwer JG, Blom JG, Furzeland RM, Zegeling PA. A moving-grid method for one-dimensional PDEs based on the method of lines. Technical report. Department of Numerical Mathematics, Centrum voor Wiskunde en Informatica; 1988.

Zegeling PA. Theory and application of adaptive moving grid methods. In: Tang T, Xu J, editors. Adaptive computations: theory and algorithms; 2007.

Zegeling PA, Kok HP. Adaptive moving mesh computations for reaction–diffusion systems. J Comput Appl Math 2004;168:519–28.

Zegeling PA, de Boer W, Tang H. Robust and efficient adaptive moving mesh solution of the 2-D Euler equations. Contemp Math 2005;383:419–30.